Martínez-Calvo, A., Rivero-Rodríguez, J., Scheid, B. & Sevilla, A. (2019, 26 noviembre). Natural break-up and satellite formation regimes of surfactant-laden liquid threads. Journal of Fluid Mechanics, 883.

DOI: 10.1017/jfm.2019.874

Natural break-up and satellite formation regimes of surfactant-laden liquid threads

[1] [2] [2]
[1]

[1]Grupo de Mecánica de Fluidos, Departamento de Ingeniería Térmica y de Fluidos,
Universidad Carlos III de Madrid, Av. Universidad 30, 28911 Leganés (Madrid), Spain

[2]TIPs, Université Libre de Bruxelles, C.P. 165/67, Avenue F. D. Roosevelt 50, 1050 Bruxelles,
Belgium

---

† Email address for correspondence: amcalvo@ing.uc3m.es

temporal stability analysis. The subject experienced a renaissance 50 years ago that has lasted to the present due to its central role in industrial and medical applications such as chemical reactors, ink-jet and three-dimensional printing, additive manufacturing, drug and protein encapsulation, and cytometry, to cite a few (the reader is referred to the reviews of Bogy 1979; Eggers 1997; Christopher & Anna 2007; Eggers & Villermaux 2008; Derby 2010; Anna 2016).

The theoretical approach to the study of the dynamics of jet break-up was first based on the linear stability analysis of infinite liquid threads. As already mentioned, the local temporal approach was pioneered by Rayleigh (1892). About 80 years later, the local spatial and spatiotemporal problems, in which the liquid jet moves with uniform velocity U with respect to the injector, were solved (Keller *et al.* 1973; Leib & Goldstein 1986*a*,*b*). In particular, it was demonstrated by Keller *et al.* (1973) that the spatial and temporal stability analyses are equivalent if U is sufficiently larger than the speed of small-amplitude capillary instability waves, U_σ. In the spatial setting, the latter condition means that the relative growth of the wave amplitude along one wavelength is small. Thus, in a frame of reference moving with the jet, the amplitude growth is spatially uniform to a first approximation, which explains the equivalence of the temporal and spatial approaches if $U \gg U_\sigma$. Since the wavelength of the unstable capillary waves is much larger than the unperturbed cylinder radius, $\bar{R}$, the scaling of U_σ depends on the value of the associated Reynolds number, $Re_\sigma = \rho U_\sigma \bar{R}/\mu$, where ρ and μ are the liquid density and viscosity, respectively. In the limit of Euler flow, $Re_\sigma \gg 1$, the value of U_σ is given by the balance $\sigma_0/\bar{R} \sim \rho U_\sigma^2$, where σ_0 is the surface tension, yielding $U_\sigma \sim \sqrt{\sigma_0/(\rho\bar{R})}$, usually referred to as the *capillary velocity*, and $U/U_\sigma \sim \sqrt{We}$, where $We = \rho U^2 \bar{R}/\sigma_0$ is the Weber number. Note that, in this case, $Re_\sigma = \sqrt{La} \gg 1$, where $La = \rho\bar{R}\sigma_0/\mu^2$ is the Laplace number, which may also be written as $La = Oh^{\ 2}$ in terms of the usual Ohnesorge number, $Oh = \mu/\sqrt{\rho\bar{R}\sigma_0}$. In the opposite limit of Stokes flow, $Re_\sigma \ll 1$, the appropriate balance is $\sigma_0/\bar{R} \sim \mu U_\sigma/\bar{R}$, whence $U_\sigma \sim \sigma_0/\mu$, usually referred to as the visco-capillary velocity. In this limit, $U/U_\sigma \sim Ca$, where $Ca = \mu U/\sigma_0$ is the capillary number, and $Re_\sigma = La \ll 1$. Therefore, the condition that must be satisfied for the temporal and spatial approaches to be equivalent is that $\sqrt{We} \gg 1$ when $\sqrt{La} \gg 1$, or that $Ca \gg 1$ when $La \ll 1$. It is also important to point out that the formation of a slender jet from a nozzle requires that $We > We_c \sim O(1)$ when $\sqrt{La} \gg 1$, or that $Ca > Ca_c \sim O(1)$ when $La \ll 1$, where We_c and Ca_c are the critical Weber and capillary numbers for the transition from convective to absolute instability (Leib & Goldstein 1986*a*,*b*).

Many experimental studies have been carried out, from the first investigations of Savart (1833), Magnus (1859), Plateau (1873), Rayleigh (1882), and Donnelly & Glaberson (1966), to the highly accurate measurements of González & García (2009), whose aim was to describe the mechanism of instability and to measure the growth rate of the associated waves in the linear regime. These experiments have shown an excellent agreement with the dispersion relation obtained by Rayleigh (Rayleigh 1878, 1892) and by Chandrasekhar (1961). It is important to emphasise that, although linear stability theory cannot describe the final stages of the dynamics prior to pinch-off, it can be used to predict the break-up time $\bar{t}_b$ with small relative errors, provided that the initial amplitude of the disturbance, ε, satisfies $\epsilon = \varepsilon/\bar{R} \ll 1$. In the spatial setting, this fact can be used to estimate the break-up length as $U\bar{t}_b$, in close agreement with experiments (Kalaaji *et al.* 2003; González & García 2009).

However, to describe the satellite formation process, which is the main objective of the present study, a nonlinear approach is needed. In particular, Goedde & Yuen (1970)

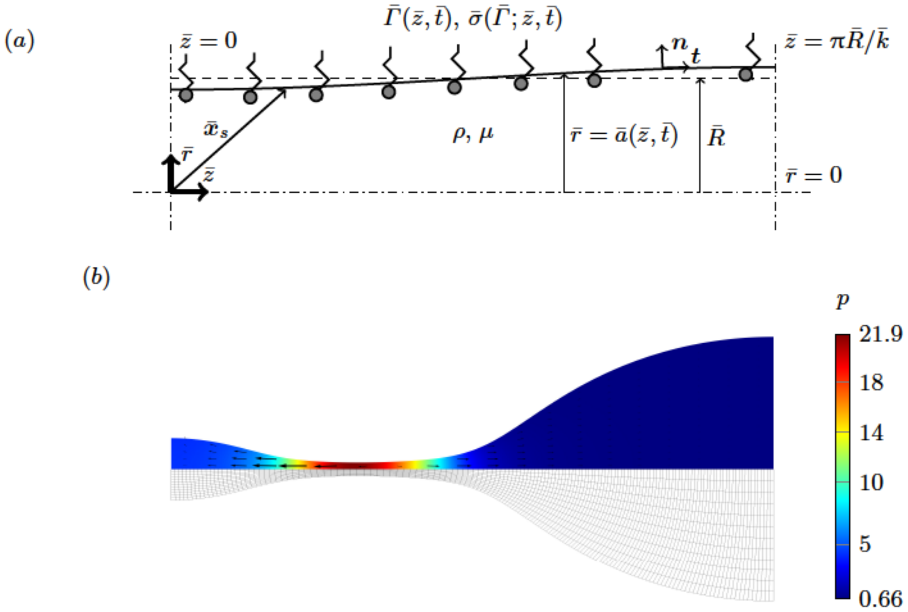

Figure 1: (Colour online) (*a*) Dimensional sketch of the flow configuration. (*b*) Example of a liquid thread approaching pinch-off for $La = 0.01$, $\beta = 1$, $\epsilon = 10^{\;3}$ and $k = k_m = 0.516$ at time $t = 123$. The contour map represents the dimensionless pressure field p, and the arrows show the dimensionless velocity field $\boldsymbol{u}$, both at the top, while the deformed mesh is shown at the bottom.

are small, namely $\mathscr{B}_\mu = \mu_s/(\mu\bar{R}) \ll 1$ and $\mathscr{B}_\kappa = \kappa_s/(\mu\bar{R}) \ll 1$ (Martínez-Calvo & Sevilla 2018). The problem is non-dimensionalised with the visco-capillary time, $\mu\bar{R}/\sigma_0$, as characteristic time and with $\bar{R}$ as characteristic length, σ_0 being the surface tension associated with the initial concentration of insoluble surfactant at the interface $\bar{\Gamma}(\bar{z},0) = \Gamma_0$, which are used to scale the surface tension and the surface concentration, respectively.

The flow is governed by the dimensionless Navier-Stokes equations

$$\boldsymbol{\nabla}\cdot\boldsymbol{u} = 0 \qquad \text{at } \mathcal{V}, \tag{2.1}$$

$$La\left(\frac{\partial\boldsymbol{u}}{\partial t} + \boldsymbol{u}\cdot\boldsymbol{\nabla}\boldsymbol{u}\right) = \boldsymbol{\nabla}\cdot\boldsymbol{T} \qquad \text{at } \mathcal{V}, \tag{2.2}$$

where $\boldsymbol{u}(\boldsymbol{x},t) = u\,\boldsymbol{e}_r + w\,\boldsymbol{e}_z$ is the velocity field, and u, w, and $\boldsymbol{e}_r$, $\boldsymbol{e}_z$ are the radial and axial velocity components and the corresponding unit vectors, respectively. In equation (2.2), $\boldsymbol{T} = -p\boldsymbol{I} + [\boldsymbol{\nabla}\boldsymbol{u} + (\boldsymbol{\nabla}\boldsymbol{u})^{\mathrm{T}}]$ is the stress tensor for an incompressible Newtonian liquid, $\boldsymbol{I}$ is the standard identity tensor and $p(\boldsymbol{x},t)$ is the pressure field. The numerical simulations reported herein were performed using an arbitrary Lagrangian–Eulerian (ALE) method, in which the domain $\boldsymbol{x}(\boldsymbol{X},t) \in \mathcal{V}(t)$ is parametrised by the initial position $\boldsymbol{X} = \boldsymbol{x}(\boldsymbol{X},0) \in \mathcal{V}(0)$, defining a time-dependent displacement field, $\boldsymbol{x}-\boldsymbol{X}$ which is enforced to satisfy the Laplace equation with proper boundary conditions specified below. The local time derivatives are evaluated in the spatial reference frame as

$$\frac{\partial\boldsymbol{u}}{\partial t} = \frac{\partial\hat{\boldsymbol{u}}}{\partial t} - \frac{\partial\boldsymbol{x}}{\partial t}\cdot\boldsymbol{\nabla}\boldsymbol{u} \qquad \text{at } \mathcal{V}, \tag{2.3}$$

where $\hat{\boldsymbol{u}}(\boldsymbol{X},t)=\boldsymbol{u}(\boldsymbol{x},t)$ is the velocity in the material reference frame.

Since the interface $\partial\mathcal{V}$ is coated with surfactant, a surface transport equation is needed for $\varGamma(\boldsymbol{x},t)$:

$$\frac{\partial \varGamma}{\partial t}+\boldsymbol{\nabla}_s\cdot(\varGamma\,\boldsymbol{u}_s)=0 \qquad \text{at } \partial\mathcal{V}, \tag{2.4}$$

where $\boldsymbol{u}_s=\boldsymbol{u}(\boldsymbol{x}_s)$ is the liquid velocity at the interface and $\boldsymbol{x}_s$ represents any position at the surface $\boldsymbol{x}_s(\boldsymbol{X}_s,t)\in\partial\mathcal{V}(t)$, which is parametrised by its initial position $\boldsymbol{X}_s=\boldsymbol{x}_s(\boldsymbol{X}_s,0)\in\partial\mathcal{V}(0)$. Here $\boldsymbol{\nabla}_s=\boldsymbol{I}_s\cdot\boldsymbol{\nabla}$ is the surface gradient operator, where $\boldsymbol{I}_s=\boldsymbol{I}-\boldsymbol{n}\boldsymbol{n}$ is the surface projection tensor and $\boldsymbol{n}$ is the outer unit normal vector at the surface. The local time derivatives at the interface are evaluated in the spatial reference frame as

$$\frac{\partial \varGamma}{\partial t}=\frac{\partial \hat{\varGamma}}{\partial t}-\frac{\partial \boldsymbol{x}_s}{\partial t}\cdot\boldsymbol{\nabla}_s\varGamma \qquad \text{at } \partial\mathcal{V}, \tag{2.5}$$

where $\hat{\varGamma}(\boldsymbol{X}_s,t)=\varGamma(\boldsymbol{x}_s,t)$ is the concentration of surfactant in the material frame of reference, which is needed in order to be implemented with the ALE method that is used in the present work. The reader is referred to the works of Stone (1990), Wong *et al.* (1996) and Pereira & Kalliadasis (2008) for further details of the time derivative of a surface quantity.

Note that the surface diffusion of surfactant has been neglected in the transport equation (2.4). Indeed, in the present work we only consider the limit where the surface Péclet number $Pe_s=U_{sc}\bar{R}/D_s\to\infty$, where D_s is the surface diffusion coefficient and U_{sc} is the characteristic liquid velocity at the free surface. The correct scaling for U_{sc} depends on the value of La. In the limit of dominant inertia, $La\gg 1$, the appropriate velocity scale is the capillary velocity, $[\sigma_0/(\rho\bar{R}^3)]^{1/2}$, so that $Pe_s=[\sigma_0\bar{R}/(\rho D_s^2)]^{1/2}$. For instance, if we consider a water thread of radius within the range 1–100 μm, the corresponding Laplace numbers lie in the range $10^2\lesssim La\lesssim 10^4$. Typical values of D_s for SDS, SB12 and other monomers in aqueous solution are within the range $10^{-9}\lesssim D_s\lesssim 10^{-8}$ m^2 s^{-1} when $\varGamma$ is below the critical micelle concentration (CMC) (Siderius *et al.* 2002), providing values of the surface Péclet number in the range $10^4\lesssim Pe_s\lesssim 10^5$. Therefore, in configurations where $La\gg 1$, it is expected that surface diffusion has a very small effect. In the opposite limit of dominant viscous forces, $La\lesssim 1$, the appropriate velocity scale is the visco-capillary velocity, σ_0/μ, leading to $Pe_s=\sigma_0\bar{R}/(\mu D_s)$. Considering, for instance, a polydimethylsiloxane silicon oil of dynamic viscosity in the range 0.1–10 Pa s, density $\rho\approx 970$ kg m^{-3} and surface tension $\sigma_0\approx 21.1$ mN m^{-1}, the Laplace number takes values in the range $10^{-4}\lesssim La\lesssim 1$. Although we are not aware of experimental studies reporting typical values of D_s in highly viscous solutions, if we assume that they are of the same order of magnitude as those of aqueous solutions, the Péclet number lies in the range $1\lesssim Pe_s\lesssim 10^6$. It is thereby deduced that, when $La\lesssim 1$, there may be cases where surface diffusion cannot be neglected in the analysis. Therefore, although the influence of surface diffusion on the satellite droplet formation process is not addressed in the present work, it clearly deserves further study, particularly in the case of highly viscous threads.

The presence of surfactant at the interface modifies σ by decreasing its value as $\varGamma$ increases, and thus the stress balance at the interface takes the following form in the limit $\mathscr{B}_\mu\ll 1$, $\mathscr{B}_\kappa\ll 1$ (Martínez-Calvo & Sevilla 2018):

$$\boldsymbol{T}\cdot\boldsymbol{n}=\boldsymbol{\nabla}_s\sigma-\boldsymbol{n}(\boldsymbol{\nabla}_s\cdot\boldsymbol{n})\sigma \qquad \text{at } \partial\mathcal{V}, \tag{2.6}$$

where the viscous stress exerted by the ambient fluid on the interface has been neglected and the ambient pressure p_a has been set to zero without loss of generality. Additionally,

T —

the temporal approach adopted herein we only consider half a perturbation wavelength subjected to the following symmetry conditions:

$$w = 0, \quad \frac{\partial u}{\partial z} = 0, \quad \text{and} \quad \frac{\partial \Gamma}{\partial z} = 0 \qquad \text{at } z = 0, \pi/k. \tag{2.12}$$

where k is the dimensionless axial wavenumber, together with the axisymmetry condition

$$\frac{\partial w}{\partial r} = 0, \quad \text{and} \quad u = 0 \qquad \text{at } r = 0. \tag{2.13}$$

Finally, regarding the initial conditions imposed at $t = 0$, we perturb the position of the liquid cylinder with a harmonic disturbance of amplitude ϵ:

$$\boldsymbol{x}_s = z\boldsymbol{e}_z + [R - \epsilon\cos(kz)]\boldsymbol{e}_r, \tag{2.14}$$

where $R = (1 - \epsilon^2/2)^{1/2}$ is a dimensionless radius defined in terms of ϵ, such that the liquid volume remains constant as ϵ varies (Ashgriz & Mashayek 1995). We also assume that the liquid thread is initially at rest and that the surfactant concentration is uniform

$$\boldsymbol{u}(\boldsymbol{x}, 0) = \boldsymbol{0}, \quad \Gamma(\boldsymbol{x}_s, 0) = 1. \tag{2.15}$$

Note that the assumption of a uniform initial concentration of surfactant is a good approximation, since our main results have been obtained in the limit $\epsilon \ll 1$ in which the deviations from a uniform concentration can be neglected. As explained in §1, our results can also be applied to describe the spatial instability and subsequent downstream break-up of liquid jets moving with uniform velocity U with respect to the injector reference frame, provided that $U \gg U_\sigma$, where U_σ is the speed of small-amplitude capillary waves. If the latter condition is satisfied, the spatial evolution of the jet is obtained by the downstream advection of the temporal results presented herein with a uniform velocity U. In particular, the jet break-up length is given by $U\bar{t}_b$ to a first approximation.

The problem depends on four dimensionless parameters, namely the Laplace number, La, the elasticity parameter, β, the axial wavenumber, k, and the amplitude of the initial perturbation, ϵ. However, in the present work we are concerned with the unforced break-up of cylindrical threads due to small-radius disturbances. Therefore, all the results were obtained by setting $k = k_m$, where $k_m(La, \beta)$ is the most unstable wavenumber (see §3.1). Moreover, it will be shown that, in the small-disturbance limit, $\epsilon \ll 1$, the only result that depends on ϵ is the break-up time of the thread, $t_b(La, \beta, \epsilon)$. However, our results have revealed that the functional dependence of t_b can be split into a contribution predicted by linear theory in explicit form, $t_{b,L}(La, \beta, \epsilon)$, plus a nonlinear correction, $\Delta t_{\mathrm{NL}}(La, \beta)$, which does not depend on ϵ. Consequently, only two independent dimensionless parameters appear in our formulation, namely La and β.

To perform the numerical simulations, the liquid domain $0 \leqslant r \leqslant a(z,t), 0 \leqslant z \leqslant \pi/k$ is partitioned into a rectangular or triangular finite-element mesh which is dynamically deformed using the ALE method. In particular, the displacement field, $\boldsymbol{x} - \boldsymbol{X}$, is enforced to satisfy the Laplace equation, and the normal mesh velocity, $\boldsymbol{n}\boldsymbol{n}\cdot\boldsymbol{u}$, solves the kinematic condition (2.7). To that end, equations (2.1)–(2.4), together with the boundary and initial conditions (2.12)–(2.15), are written in weak form following the methodology described by Rivero-Rodríguez & Scheid (2018*a*,*b*), and the spatial discretisation is carried out using the finite-element method (FEM) provided by COMSOL, where Lagrange linear (P1) elements are used for p and quadratic (P2) elements are used for $\boldsymbol{x}$, $\boldsymbol{u}$ and Γ. The time discretisation was performed using the first-order backward Euler method with adaptive time stepping. Figure 1(*b*) shows a representative deformed mesh for a simulation with $La = 0.01$, $\beta = 1$, $\epsilon = 10^{\;3}$ and $k = k_m = 0.516$ at time $t = 123$, together with the pressure field as a contour plot and the velocity field represented by arrows. All the results reported were carefully checked as being mesh-independent, with an integration tolerance of the order of 10^{-6}–10^{-7}. In addition, it was checked that the relative variations of liquid volume and surfactant mass where smaller than 10^{-5} during each simulation. The numerical code has been validated with the linear theory in §3.1. In the nonlinear regime, the validation was performed by comparing our results with those of Ashgriz & Mashayek (1995) for a clean interface and with those of McGough & Basaran (2006) and Kamat *et al.* (2018) for a surfactant-laden thread (not shown). In particular, the Appendix is devoted to show the performance of our numerical framework close to pinch-off, comparing our results with the different theoretical scalings of the minimum radius as a function of time to break-up.

3. Results and discussion

Since we are interested in the spontaneous break-up of the surfactant-laden thread, all the results were computed from an initial condition where the liquid cylinder is perturbed with the wavenumber of maximum amplification, $k_m(La, \beta)$. Hence, the results of a linear stability analysis are first summarised in §3.1 to obtain k_m and ω_m, the latter being the maximum temporal growth rate. Note that k_m is needed to define the initial geometry and the initial condition (2.14), while ω_m is used to compute the nonlinear correction to the linear break-up time, which is defined in §3.2. In addition, the linear theory has also been used to validate the numerical code by comparing the associated maximum temporal growth rate, ω_m, with the results extracted from the numerical simulations during the initial transient of exponential amplitude growth. Sections §3.2 and 3.3 are devoted to the analysis of the nonlinear break-up and the satellite formation dynamics, separating the weak-elasticity limit, and the surfactant-laden case. To that end, we have performed direct numerical simulations of equations (2.1)–(2.15) until times very close to pinch-off. In particular, we report a parametric study for different values of La and β, computing the volume of the satellite droplet, the mass of surfactant trapped at its interface, the satellite shape at pinch-off, and the break-up time.

At this point, it has to be pointed out that a similar phenomenology was previously reported by Dravid *et al.* (2006) for $La = 0.01$ and 100, although using the linearised equation of state $\sigma(\varGamma) = 1 - \beta(\varGamma - 1)$. In addition, those authors did not consider the natural break-up of the thread, since the disturbance wavenumber k was restricted to fixed values different from the most amplified one, k_m.

3.1. *Linear stability analysis*

To obtain the dispersion relation $D(\omega, k) = 0$ relating the temporal growth rate ω and the axial wavenumber k, all the flow variables are slightly perturbed around a uniform stationary state and decomposed as temporal normal modes:

$$(u, w, p, a, \sigma, \varGamma) = (0, 0, 1, 1, 1, 1) + \epsilon(\hat{u}, \hat{v}, \hat{p}, \hat{a}, \hat{\sigma}, \hat{\varGamma}) \exp(ikz + \omega t). \tag{3.1}$$

Introducing (3.1) into the system (2.1)–(2.4) and keeping terms proportional to ϵ, the following dispersion relation is obtained:

$$\begin{aligned} &La\,\omega^2 F(k) - k^2(1 - k^2) + \beta k^2[1 + F(k)(F(\tilde{k}) - 2)] \\ &+ \frac{k^4}{La}\left[4 - \frac{\beta}{\omega}\left(2 - \frac{1 - k^2}{\omega}\right)\right][F(k) - F(\tilde{k})] + 2\omega k^2(2F(k) - 1) = 0, \end{aligned} \tag{3.2}$$

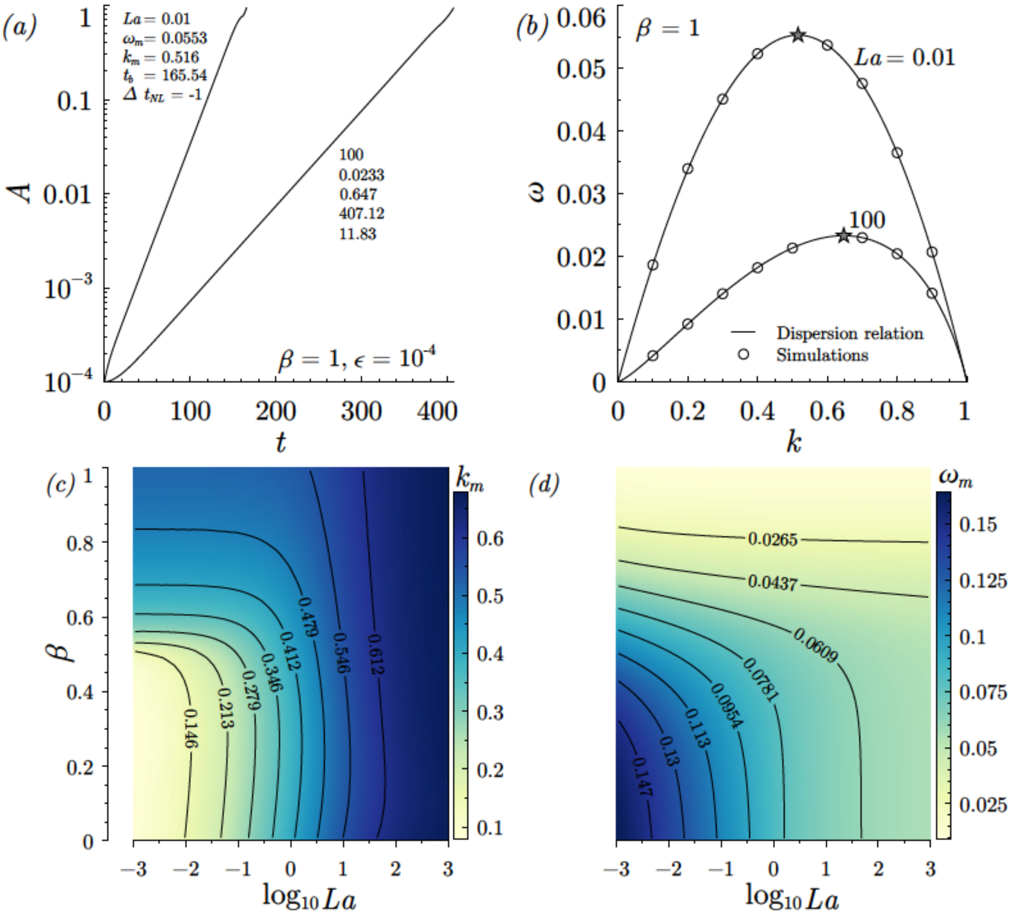

Figure 2: (Colour online) (*a*) Semi-logarithmic plot of the radius amplitude $A(t)$ as a function of time, extracted from two numerical simulations for $\epsilon = 10\ {}^{4}$, $\beta = 1$ and two values of the Laplace number, namely $La = (0.01, 100)$. The corresponding optimal wavenumbers, $k_m(La, \beta)$, highlighted in (*b*) with stars, are used to build the initial conditions, and their values are indicated near each curve together with the associated linear temporal growth rates, $\omega_m(La, \beta)$ and La. (*b*) Temporal growth rate ω as a function of the axial wavenumber k, computed with the dispersion relation (3.2) (solid lines) and with the numerical simulations (circles), for $\beta = 1$ and two different values of $La = (0.01, 100)$, indicated near each curve. The maximum growth rates ω_m computed in (*a*) are marked with stars. (c) Isocontours of the most amplified wavenumber $k_m(La, \beta)$ and its corresponding growth rate $\omega_m(La, \beta)$ in (*d*).

where $\tilde{k} = \sqrt{k^2 + La\,\omega}$ and $F(x) = xI_0(x)/I_1(x)$. Here, $I_n(x)$ denotes the nth-order modified Bessel function of the first kind. Note that dispersion relation (3.2) is exactly the same as the one deduced by Timmermans & Lister (2002), and is also a particular case of the one provided by Martínez-Calvo & Sevilla (2018) in the limit of negligible surface viscosities. The Rayleigh–Chandrasekhar dispersion relation is recovered when $\beta \to 0$ (Rayleigh 1892; Chandrasekhar 1961).

As shown experimentally by Goedde & Yuen (1970), and numerically by Mansour & Lundgren (1990) and Ashgriz & Mashayek (1995), a convenient way to compute the temporal growth rate of small disturbances is through the radius amplitude, extracted from the present simulations as $A(t) = (\max_z[a(z,t)] - \min_z[a(z,t)])/2$. Figure 2($a$) shows the temporal evolution of $A(t)$ in semi-logarithmic scale, extracted from two numerical simulations for an initial perturbation amplitude $\epsilon = 10^{-4}$, an elasticity parameter $\beta = 1$, and two values of the Laplace number, $La = 0.01$ and $La = 100$, close to the Stokes and Euler regimes, respectively. In each case, the most amplified wavenumber, $k_m(La, \beta)$, is used to build the initial condition. As expected due to the smallness of ϵ, figure 2(a) shows that during most of the time the amplitude grows exponentially, i.e. $A \propto \exp(\omega_m t)$, and thus the maximum temporal growth rate, $\omega_m(La, \beta)$, can be easily computed as the slope of the linear region in the semi-logarithmic plot, $\omega_m = \mathrm{d}\ln(A)/\mathrm{d}t$. It can also be deduced from figure 2(a) that there is an initial transient during which the growth of $A(t)$ is not exponential, which can be explained by the fact that the initial conditions in the numerical simulations are imposed on the shape of the interface, but disregard the associated disturbances in the velocity, pressure and surfactant concentration fields. As shown in figure 2(b), this procedure was used to obtain ω for different values of k (symbols), and the results are compared with the amplification curves $\omega(k)$ computed from the dispersion relation (3.2) (solid lines), affording an excellent agreement that validates the numerical code in the linear regime. Finally, figures 2(c, d) show the isocontours of k_m and ω_m, respectively, as a function of La and β extracted from equation (3.2), whose values will be used hereafter.

3.2. *Satellite formation regimes and transitions in the* (La, β) *parameter plane*

Let us first present the structure of the (La, β) parameter plane in terms of the satellite formation process. To that end, we conducted an exhaustive parametric study in which the Laplace and elasticity parameters were varied in small steps within wide ranges, namely $0.01 \leqslant La \leqslant 100$ and $0 \leqslant \beta \leqslant 1$. Thus, for each pair of values of La and β, we simulated the instability-driven time evolution of the thread from an initial condition with $\epsilon \ll 1$ until a time t_b very close to break-up. In total, around 10^4 time-dependent simulations were carried out to characterise the (La, β) parameter plane shown in figures 3 and 5.

At this point, it is important to emphasise that the fate of the main and satellite drops after pinch-off is outside the scope of the present work, and therefore we do not explore the possible successive break-up events that may take place and lead to the formation of sub-satellites. Keeping this in mind, we have extracted the satellite volume at the last numerical step, $t = t_b$. Normalising its value with the total volume provides the definition

$$V_{\mathrm{sat}} = \frac{\int_0^{z_{\mathrm{min}}} a^2 \mathrm{d}z}{\int_0^{\pi/k_m} a^2 \mathrm{d}z}, \tag{3.3}$$

where z_{min} is the axial position where the liquid column reaches its minimum radius, a_{min}, at $t = t_b$. A more common measure of the satellite size is its equivalent radius, R_{sat}, which is the radius of a spherical drop of the same volume as the satellite (Rutland & Jameson 1971; Mansour & Lundgren 1990; Ashgriz & Mashayek 1995; Mashayek & Ashgriz 1995). All the results reported herein in terms of V_{sat} can be easily converted to R_{sat} through the equation $R_{\mathrm{sat}} = [3\pi V_{\mathrm{sat}}/(2k_m)]^{1/3}$. Following the same procedure, we have also computed the mass of surfactant trapped at the satellite surface which,

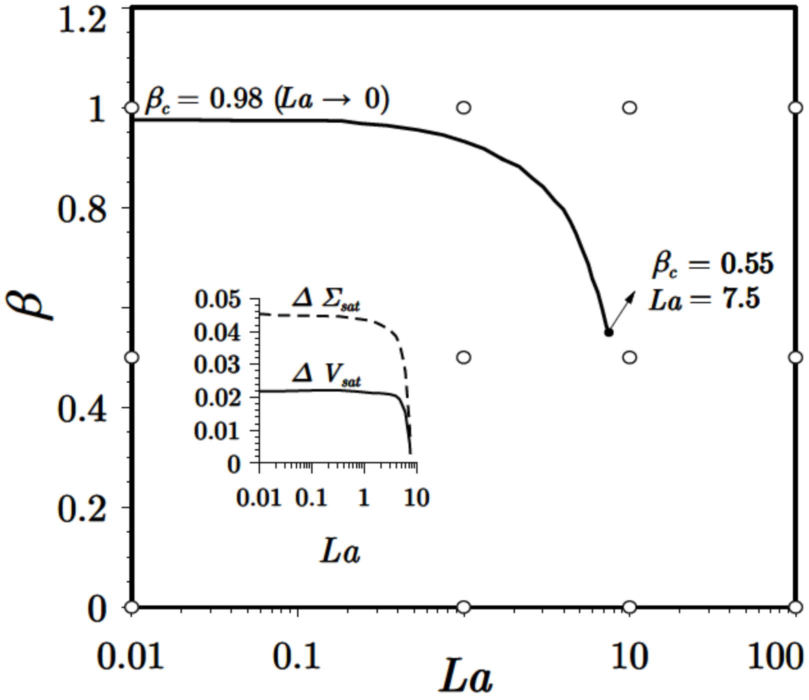

Figure 3: The structure of the (La, β) parameter plane. An abrupt transition takes place along the solid line, $\beta = \beta_c(La)$, across which both the satellite volume and the entrapped mass of surfactant experience a discontinuous jump, such that both magnitudes are larger above the solid line. The inset shows the jumps in the satellite volume, $\varDelta V_{\text{sat}}(La) = V_{\text{sat}}(\beta - \beta_c \to 0^{+}) - V_{\text{sat}}(\beta - \beta_c \to 0^{\ \ })$, and in the associated entrapped mass of surfactant, $\varDelta \varSigma_{\text{sat}}$. Both jumps, together with β_c, increase monotonically as La decreases, and reach respective Stokes asymptotes as $La \to 0$, namely $\varDelta V_{\text{sat}} \to 0.022$, $\varDelta \varSigma_{\text{sat}} \to 0.045$, and $\beta_c \to 0.98$. The filled circle indicates the origin of the discontinuous transition, $(La, \beta_c) = (7.5, 0.55)$, at which both jumps become zero. For $La > 7.5$, the satellite volume is a continuous function of β. The open circles correspond to the values of La and β of the shapes just before pinch-off shown in figure 4.

normalised with the total mass of surfactant, provides the definition

$$\varSigma_{\text{sat}} = \frac{\int_0^{z_{\min}} a\varGamma \sqrt{1 + \left(\frac{\partial a}{\partial z}\right)^2} \mathrm{d}z}{\int_0^{\pi/k_m} a\varGamma \sqrt{1 + \left(\frac{\partial a}{\partial z}\right)^2} \mathrm{d}z}. \tag{3.4}$$

We point out that, since V_{sat} and $\varSigma_{\text{sat}}$ are always obtained when $a_{\min}$ is within the range $a_{\min} \sim 10^{\ \ 4} - 8 \times 10^{\ \ 3}$, the sensitivity of these magnitudes to the exact value of $a_{\min}$ is negligible, such that both represent very robust measures. Similarly, the corresponding break-up time t_b is barely sensitive to the value of $a_{\min}$.

In contrast with V_{sat} and $\varSigma_{\text{sat}}$, which do not depend on the initial amplitude in the limit $\epsilon \ll 1$, the break-up time is a function of the form $t_b(La, \beta, \epsilon)$ such that $t_b \to \infty$ as $\epsilon \to 0$. Indeed, the break-up time can be easily estimated from linear theory through the equation $a_{\min}(t) \sim 1 - \epsilon \exp(\omega_m t)$, where ω_m is the growth rate associated with the most amplified wavenumber k_m shown in figures 2 (c, d), leading to the estimation

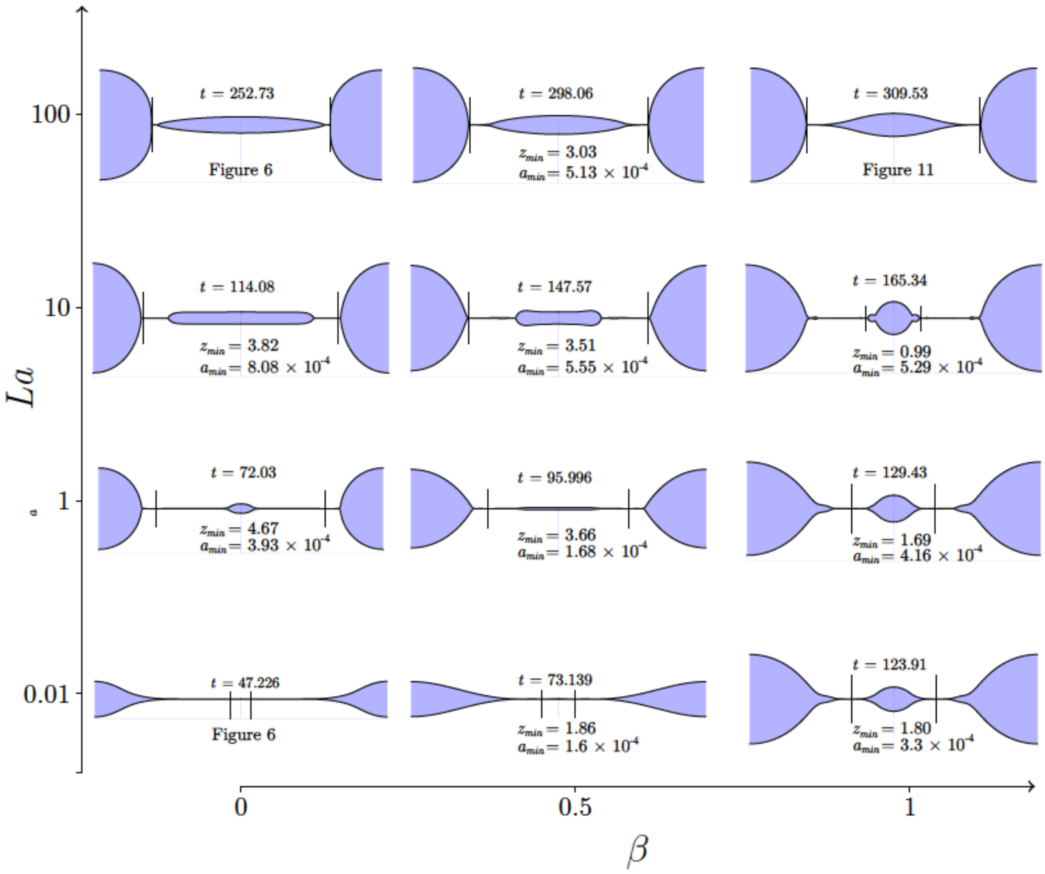

Figure 4: (Colour online) The satellite shapes just prior to pinch-off in the (La, β) parameter plane (see open circles in figure 3). The vertical lines indicate the axial positions, $z_{\min}$, of the minimum thread radii, $a_{\min}$.

$t_b \sim \ln(\epsilon\ ^{1})/\omega_m$. Based on the latter result, we define the nonlinear correction to the linear break-up time as

$$\Delta t_{\mathrm{NL}} = t_b - \frac{\ln(\epsilon\ ^{1})}{\omega_m}, \tag{3.5}$$

where t_b is obtained by extrapolating $a_{\min}$ to zero using the last few computed time steps. Unlike t_b, Δt_{NL} only depends on La and β, but not on ϵ, provided only that $\epsilon \ll 1$. The latter fact is demonstrated in §3.3. Finally, we have also computed the sphericity of the satellite droplet at pinch-off as

$$\mathcal{S} = \frac{2\left(\frac{3}{4}\int_0^{z_{\min}} a^2 \mathrm{d}z\right)^{2/3}}{\int_0^{z_{\min}} a\sqrt{1 + \left(\frac{\partial a}{\partial z}\right)^2}\mathrm{d}z}, \tag{3.6}$$

which is the ratio between the surface of a sphere of the same volume as the satellite and its actual surface. The quantification of the satellite formation process will be based on the four functions V_{sat}, Σ_{sat}, Δt_{NL} and $\mathcal{S}$, extracted from the numerical simulations. These four functions only depend on La and β when ϵ is sufficiently small, as is demonstrated in §3.3. Thus, the main results reported herein have been computed in the limit $\epsilon \to 0$.

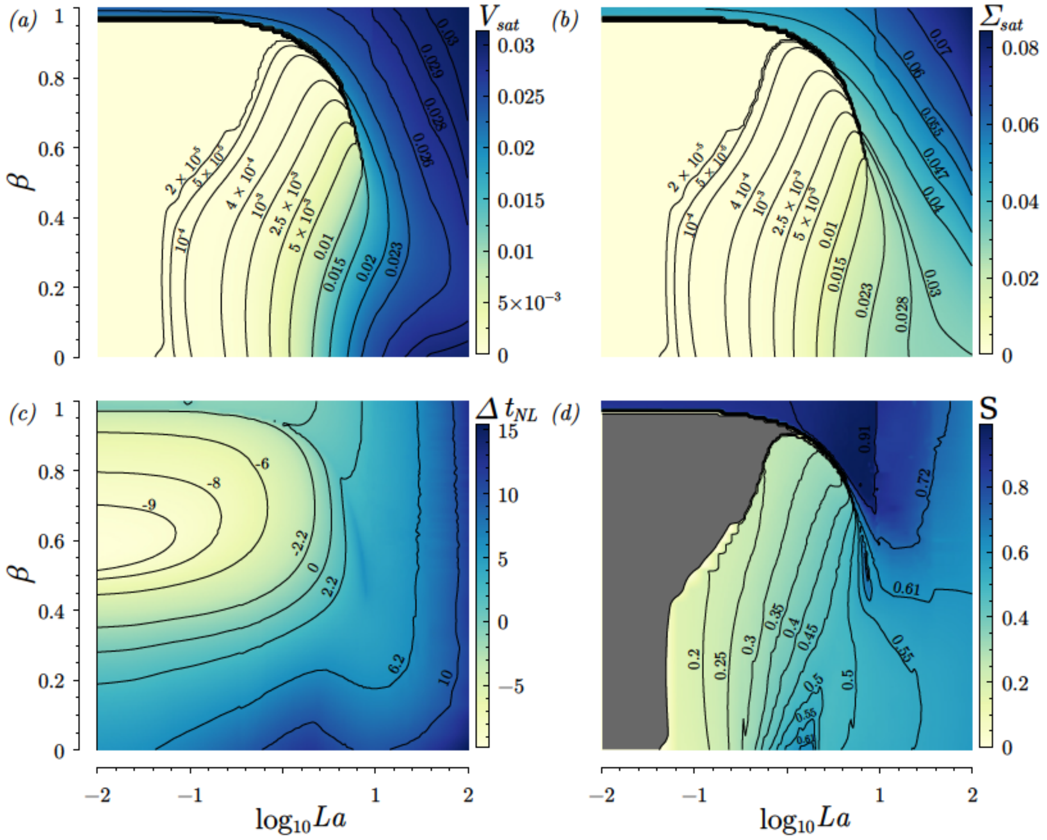

Figure 5: (Colour online) Isocontours in the (La, β) parameter plane of (a) the normalised satellite volume V_{sat}, (b) the normalised mass of surfactant trapped at its interface Σ_{sat}, (c) the nonlinear correction to the break-up time, Δt_{NL}, and (d) the sphericity of the satellite droplet, $\mathcal{S}$.

The structure of the (La,β) parameter plane is summarised in figures 3 and 4 in terms of the satellite formation process. In particular, figure 3 depicts the most salient features of the parameter plane, and figure 4 displays several satellite shapes at the last computed numerical step just prior to pinch-off, whose associated values of La and β are indicated with circles in figure 3. The most important feature of the parameter plane is the solid line shown in figure 3, which represents a discontinuous transition that takes place for a critical elasticity, $\beta = \beta_c(La)$ for $La < 7.5$. In particular, both the satellite volume and the associated entrapped mass of surfactant experience sudden jumps from certain values $V_{\mathrm{sat}}(\beta-\beta_c \to 0\ \ )$ and $\Sigma_{\mathrm{sat}}(\beta-\beta_c \to 0\ \ )$ to larger values $V_{\mathrm{sat}}(\beta-\beta_c \to 0^+)$ and $\Sigma_{\mathrm{sat}}(\beta-\beta_c \to 0^+)$. Indeed, the inset of figure 3 shows the jumps experienced by the satellite volume, $\Delta V_{\mathrm{sat}}(La) = V_{\mathrm{sat}}(\beta-\beta_c \to 0^+) - V_{\mathrm{sat}}(\beta-\beta_c \to 0\ \ )$, and by the associated entrapped mass of surfactant, $\Delta\Sigma_{\mathrm{sat}}$. Both jumps and β_c increase monotonically as La decreases, and reach respective Stokes asymptotes as $La \to 0$, namely $\Delta V_{\mathrm{sat}} \to 0.022$, $\Delta\Sigma_{\mathrm{sat}} \to 0.045$, and $\beta_c \to 0.98$. The filled circle in figure 3 indicates the origin of the discontinuous transition, $(La, \beta_c) = (7.5, 0.55)$, at which both jumps become zero. For values of $La > 7.5$, V_{sat} and Σ_{sat} are continuous functions of La and β.

As shown in figure 4, for values of $\beta = 0 < \beta_c$ and $\beta = 0.5 < \beta_c$ the sequence of interface shapes at pinch-off depends continuously on La, with the trend that larger satellites are formed as La increases, reaching the regular limit of inviscid flow as $La \to \infty$. For $\beta < \beta_c$ and small values of La, figure 4 reveals that the main drops are separated by very thin threads of tiny volume whose break-up behaviour has been characterised in previous studies (see e.g. Kowalewski 1996). For $\beta < \beta_c$ and intermediate values of La, the main drops are separated by a satellite centred at $z = 0$ that is connected to the main drops by very thin threads (see e.g. the case for $La = 1$ and $\beta = 0$ in figure 4). Finally, for $\beta < \beta_c$ and large values of La, the satellite drop is directly connected to the main drops. In contrast, when $\beta = 1 > \beta_c$, figure 4 shows a different picture, where large satellites are formed for all values of La. These results have also been analysed quantitatively, and are discussed in detail below.

From figures 3 and 4 it is deduced that, although the physical mechanisms are different, both the liquid inertia and the interfacial elastic stress favour the formation of satellites. In particular, surface elasticity tends to form spherical-shaped satellites at pinch-off, whereas the increase of the liquid inertia generates oval-shaped satellites. In the set of shapes close to pinch-off shown in figure 4, a discontinuous transition is observed for $La = 0.01$ and 1, as β increases. However, for $La = 10 > 7.5$ a continuous transition of the thread shape is observed as β increases. Finally, for $La = 100$, the upper row evidences that the influence of the elastic stress on the shape of the thread is much weaker when the value of La is large enough. The physics underlying these transitions can be explained in terms of the coupling between the liquid inertia, the viscous stress, the surface tension, and the interfacial elastic stress. The competition between these forces is discussed in §3.3, based on the trends exhibited by the functions V_{sat}, Σ_{sat}, Δt_{NL} and $\mathcal{S}$, and also by analysing the temporal evolution of the interface shapes starting from small disturbances, depending on the values of La and β.

3.3. *Nonlinear dynamics of a surfactant-laden interface: satellite drop formation*

To unveil the effect of liquid inertia, viscous stresses and surface elasticity on the satellite droplet formation regimes, here we present and discuss the quantitative results of the detailed numerical analysis that has been carried out in the present work.

Figure 5 shows the isocontours of V_{sat}, Σ_{sat}, Δt_{NL} and $\mathcal{S}$ in the (La, β) parameter plane. We first observe that, at the discontinuous transition that occurs for $La < 7.5$, the value of V_{sat} increases from 10^{-3}–1.5 % to 2–2.3 %, whereas Σ_{sat} increases from 10^{-3}–1.5 % to 3.5–4.7 %. The exact value of both jumps as functions of La can be seen in the inset of figure 3. In contrast, for $La > 7.5$ or $\beta > \beta_c(La)$, the values of V_{sat}, Σ_{sat}, Δt_{NL} and $\mathcal{S}$ vary continuously.

As a first general observation, it is deduced from figure 5 that the linear theory may either underestimate or overestimate the break-up time, in a way that does not necessarily coincide with the transitions in the satellite formation process. Indeed, t_b is underestimated for $La \gg 1$ independently of the value of β. However, for $La \ll 1$, t_b is overestimated for $0.28 \lesssim \beta \lesssim 1$, while it is underestimated outside this range. Regarding the sphericity $\mathcal{S}$, figure 5 confirms the trend deduced from figure 4: the most spherical satellite shapes, with $\mathcal{S} \gtrsim 0.9$, take place for $\beta \gtrsim \beta_c$ and $La \lesssim 10$. In contrast, the shapes become most elongated, with $\mathcal{S} \lesssim 0.2$, when $\beta < \beta_c$ and $La \lesssim 0.1$ (grey area in figure 5*d*).

3.3.1. *Analysis of the temporal evolution of clean interfaces*

To present the dynamics of satellite droplet formation, we take as reference cases the two canonical temporal evolutions of clean interfaces ($\beta = 0$) illustrated in figure 6, for $La = 0.01$ in (*a*–*d*), close to the Stokes limit, and for $La = 100$ in (*e*–*h*), an almost inviscid case close to the Euler limit (as shown in §3.3.4). Specifically, we plot snapshots

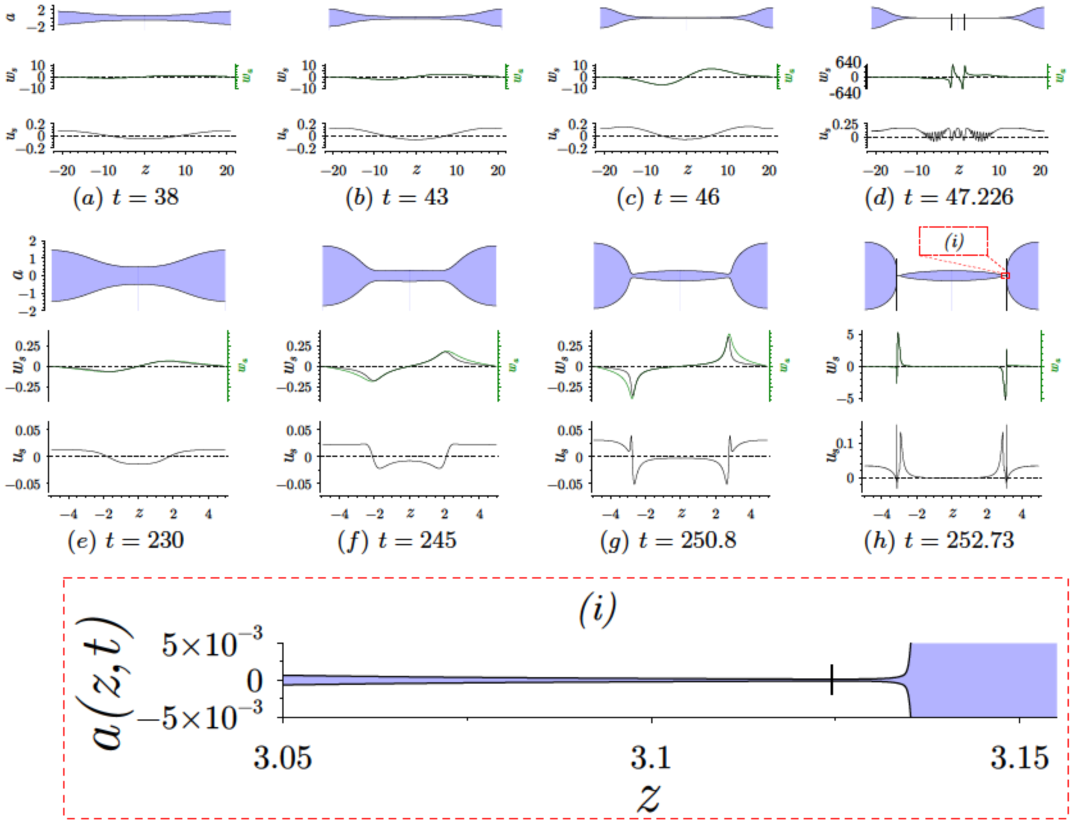

(a) $t = 38$ (b) $t = 43$ (c) $t = 46$ (d) $t = 47.226$

(e) $t = 230$ (f) $t = 245$ (g) $t = 250.8$ (h) $t = 252.73$

Figure 6: (Colour online) Temporal evolution of the liquid thread radius a (upper row), of the axial velocities at the free surface, w_s, and at the axis, w_a (middle row) and the radial surface velocity u_s (bottom row), for $\epsilon = 10^{-3}$, $\beta = 0$, $(a\text{–}d)$ $La = 0.01$, $k = k_m = 0.150$, and $(e\text{–}h)$ $La = 100$, $k = k_m = 0.635$. The vertical lines in each last snapshot indicate the axial position $z_{\min}$ of minimum radii $a_{\min}$, being $z_{\min} = 1.49$ and $a_{\min} = 3.63 \times 10^{-5}$ for $La = 0.01$, and $z_{\min} = 3.12$ and $a_{\min} = 1.29 \times 10^{-4}$ for $La = 100$. (i) Zoomed region close to the neck at the instant shown in (h).

at different times, indicated in the labels, of the jet radius a (upper rows), the axial surface velocity w_s (middle rows, black lines), the axial velocity at the centreline w_a (middle rows, green lines) and the radial surface velocity u_s (bottom rows). In both cases the initial disturbance amplitude is very small, $\epsilon = 10^{-3}$, and thus the initial evolution is triggered by the Plateau–Rayleigh instability mechanism, and can be described with linearised theory. This initial stage is not shown in figure 6 for conciseness, but it can be appreciated in figure 2(a). The initial disturbance, of most amplified wavelength k_m, creates an axial capillary pressure gradient that induces a flow from the valley to the crest of the wave. The latter mechanism finally leads to the break-up of the liquid thread and the formation of two main drops with either a liquid thread or a satellite droplet in between.

A key feature that determines the nonlinear evolution of the destabilised thread is the fact that the axial curvature makes the capillary pressure gradient to be locally larger in the regions that connect the central part of the thread with the growing crests, as

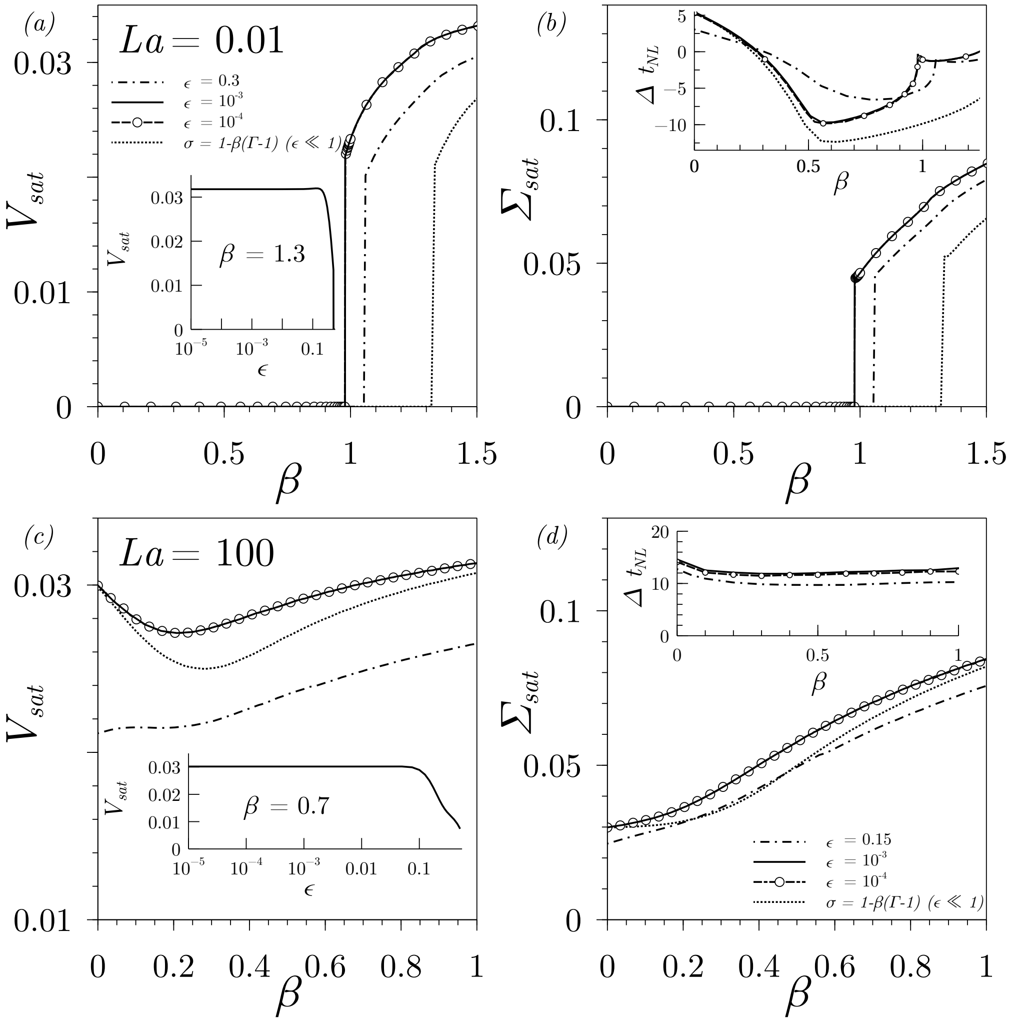
(a)
$La = 0.01$
$\epsilon = 0.3$
$\epsilon = 10^{-3}$
$\epsilon = 10^{-4}$
σ = 1-β(Γ-1) ($\epsilon \ll 1$)
V_{sat}
$\beta = 1.3$
ϵ
β
(b)
Δt_{NL}
Σ_{sat}
β
(c)
$La = 100$
V_{sat}
$\beta = 0.7$
ϵ
β
(d)
Δt_{NL}
Σ_{sat}
$\epsilon = 0.15$
$\epsilon = 10^{-3}$
$\epsilon = 10^{-4}$
σ = 1-β(Γ-1) ($\epsilon \ll 1$)
β

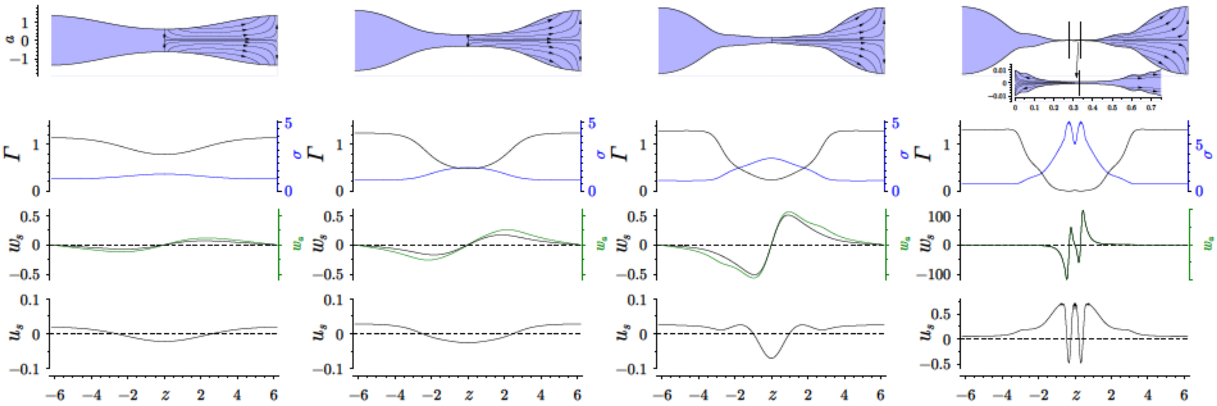

(*a*) $t = 100$ (*b*) $t = 112$ (*c*) $t = 118$ (*d*) $t = 119.03$

Figure 8: (Colour online) Temporal evolution of the liquid thread radius a (first row), surfactant concentration $\mathit{\Gamma}$ (second row, black lines), surface tension σ (second row, blue lines), axial velocity at the interface w_s (third row, black lines) and at the centreline w_a (third row, green lines), and radial surface velocity u_s (fourth row), for $La = 0.01$, $\epsilon = 10^{-3}$ and $\beta = 0.960 < \beta_c(La = 0.01)$, with $k = k_m = 0.508$. The vertical line in the last snapshot of a indicates the position of $z_{\min}$. Here $z_{\min} = 0.33$ and $a_{\min} = 7.29 \times 10^{-4}$.

(second row), the axial velocity at the interface, w_s, and at the centreline, w_a (third row), and the radial surface velocity u_s (fourth row). Time is indicated in the labels.

The presence of surfactants introduces two main effects. The advection of surfactant molecules outside the central region of the thread increases the local surface tension in this region, as can be observed in the figures 8(*a*) and 9(*a*). This surfactant depletion generates two opposed effects. First, the axial capillary pressure gradient is enhanced, since the value of σ becomes larger in the central region, where $\mathit{\Gamma}$ is smaller, while σ becomes smaller away from the centre, where $\mathit{\Gamma}$ is larger. Second, there is a stabilising effect induced by the elastic or Marangoni stress, which competes with the destabilising Plateau-Rayleigh mechanism enhanced by the first effect. Actually, the gradient of σ generates a tangential stress at the interface directed towards increasing values of σ, which opposes the drainage flow and tends to replenish the central zone with surfactant.

In the case of $\beta < \beta_c(La = 0.01)$, figure 8(*b*,*c*) shows that the Marangoni stress reduces the axial surface velocity, w_s, compared with the centreline velocity, w_a, the difference between both velocities being larger in the region where $\boldsymbol{\nabla}_s\sigma$ is higher. As the fluid is drained from the centre for increasing times, $\boldsymbol{\nabla}_s\sigma$ becomes larger. When $\beta < \beta_c(La = 0.01)$ the capillary pressure gradient is able to remove most of the liquid from the centre. Eventually, close to pinch-off, inertia becomes important and the flow is reverted close to $z = 0.33$, so that the rate of thinning increases in this region and $z_{\min}$ moves towards the latter axial position where the liquid thread finally detaches forming a tiny satellite droplet with $V_{\text{sat}} < 10^{-5}$, as evidenced by figure 8(*d*). Note that, during thread evolution, two bulges connecting the central and outer regions grow due to the reduction of the surface velocity, and are finally connected by a thin liquid thread close to pinch-off.

When $\beta > \beta_c(La = 0.01)$ the foregoing explanation still holds, but the elastic stress is large enough to revert the flow near the interface at early times far from break-up, as shown in figure 9(*a*). The associated stagnation point diffuses radially inwards, and leads

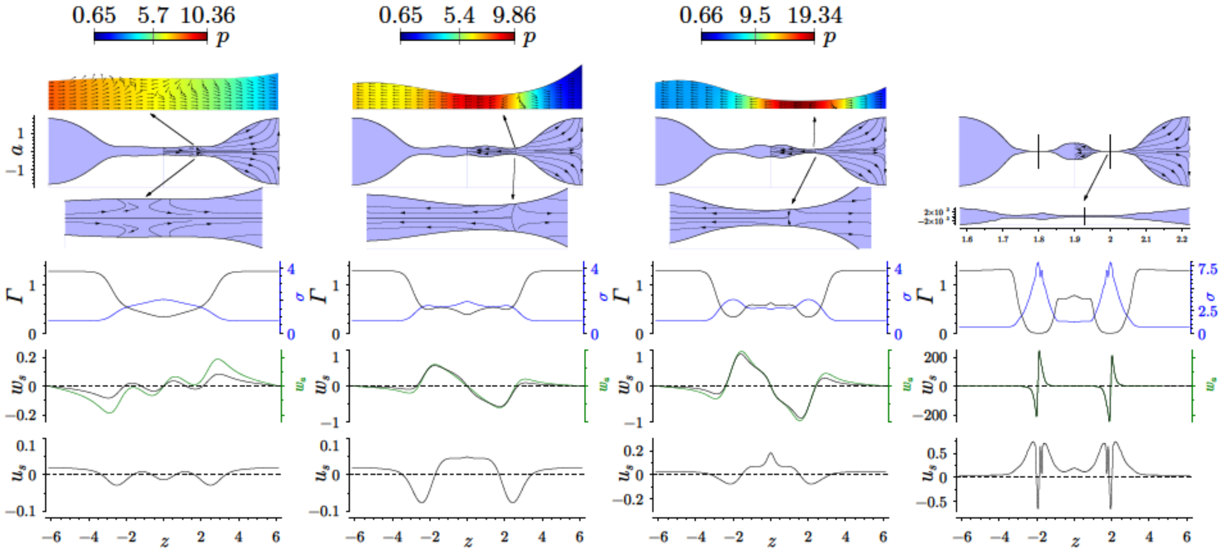

(a) $t = 119.8$ (b) $t = 122$ (c) $t = 122.8$ (d) $t = 123.7$

Figure 9: (Colour online) Same as figure 8 but for $\beta = 0.979 > \beta_c(La = 0.01)$, with $k = k_m = 0.512$. The insets are zooms showing the normalised velocity vector field and isocontours of the pressure field. Here $z_{\text{min}} = 1.93$ and $a_{\text{min}} = 2.5 \times 10^{\ 4}$.

to a counterflow separating a region where liquid flows towards the centre and induces the formation of a satellite from another region where the incipient main drop is fed with liquid. Consequently, the thread detaches in between these two regions. If β increases further, the break-up time increases and the flow reversal occurs at earlier stages, so that V_{sat} and Σ_{sat} increase monotonically, as shown in figures 7(a,b).

When $La = 100$, figures 7(c,d) show that the effect of surface elasticity is much weaker in the case of dominant inertia, as was anticipated both in figure 5 and also by the shapes shown in the upper row of figure 4. The small influence of insoluble surfactants in the inviscid limit, $La \gg 1$, had been already noted in the linear stability analyses of Whitaker (1976), Hansen *et al.* (1999) and Timmermans & Lister (2002). Indeed, the effect of Marangoni stresses is confined to a thin boundary layer at the free surface, where the viscous stress rapidly restores any imbalance of σ, and which does not have any influence in the bulk liquid motion. Consequently, for $La = 100$, the satellite volume, V_{sat}, varies only slightly with respect to the value of a clean liquid thread, $V_{\text{sat}}(\beta = 0, La = 100) \simeq 0.03$, with a minimum at $\beta \simeq 0.203$, whereas Σ_{sat} increases monotonically as β increases. To explain this result, figures 10 and 11 show two sets of snapshots of a, Γ, σ, w_s, w_a and u_s for $\beta = 0.203$, at which V_{sat} is minimum, and for $\beta = 1$, respectively.

In the weak-elastic limit, $\beta \to 0$, a satellite droplet with volume $V_{\text{sat}} \simeq 3\%$ is formed at pinch-off, as already shown in figures 5 and 7(c). The satellite volume decreases as β increases in the range $0 < \beta \lesssim 0.203$. Indeed, when β increases, the Marangoni rigidification of the interface slows down the pinch-off process by decreasing the interfacial velocities, as evidenced by the time evolution of w_s, w_a and u_s in figure 10 with respect to figure 6(e–h). The latter behaviour, together with the fact that the pressure gradient is locally enhanced due to the variations of σ, explain why a larger volume is drained out of the satellite droplet compared to the case of a clean interface. However, the Marangoni stress that opposes the drainage flow away from the centre reduces the advection of

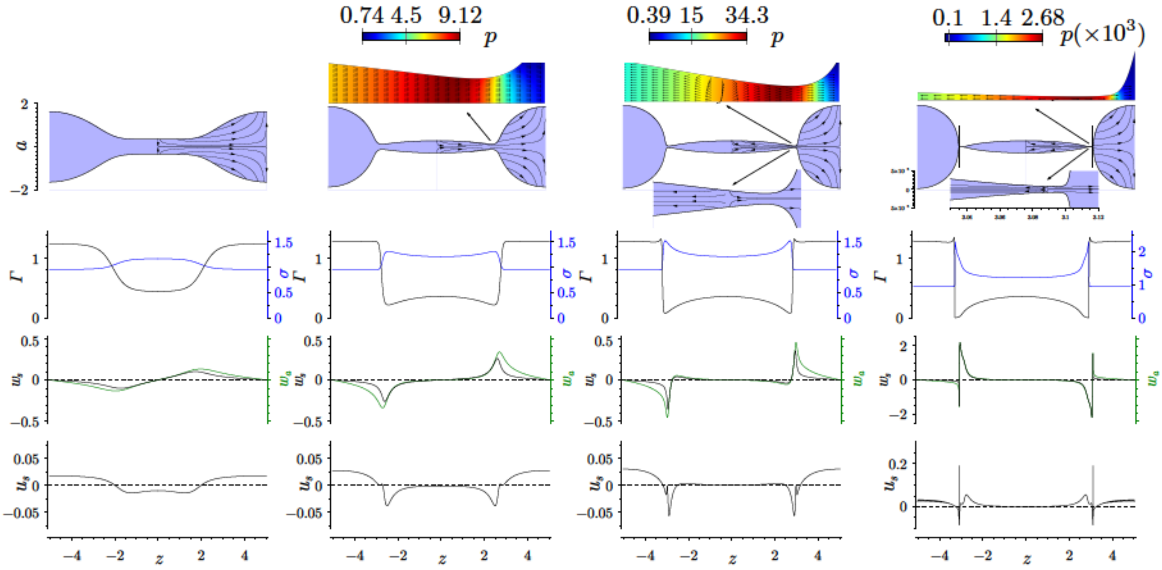

(*a*) $t = 268$ (*b*) $t = 278.5$ (*c*) $t = 280.5$ (*d*) $t = 281.06$

Figure 10: (Colour online) Same as figure 8 but for $La = 100$ and $\beta = 0.203$, with $k = k_m = 0.625$. Here $z_{\min} = 3.09$ and $a_{\min} = 7.89 \times 10^{\ 4}$.

surfactant towards the main drops, and thus the value of $\Sigma_{\rm sat}$ increases, as shown in figure 7(*d*). The snapshot in figure 10(*c*) shows that the flow is reversed near the neck region, as happens for a clean interface (see e.g. figures 6*h* and 6*i*). However, in the elastic regime the flow reversal takes place earlier than in the clean interface limit. This behaviour at high values of La and low values of β was previously noticed by Kamat *et al.* (2018), who showed that the stagnation point occurs at earlier stages in surfactant-laden interfaces compared with clean interfaces, due to the strong Marangoni stress in the neck region.

A representative case of $La = 100$ and $\beta > 0.203$ is shown in the snapshots of figure 11 for $\beta = 1$. The main change with respect to the preceding case is the fact that for $\beta = 1$ the Marangoni stress is strong enough to revert the surface flow at earlier stages, as shown in panels (*b*) and (*d*). Therefore, the stagnation point appears earlier than in the case of figure 10, and diffuses almost instantaneously in the radial direction, leading to a satellite droplet with larger values of the normalised volume and of the surfactant mass. It can thus be deduced that the minimum value of $V_{\rm sat}$ displayed in figure 7(*c*) appears due to a competition between the two aforementioned opposite effects induced by the presence of surfactants.

For $La < 7.5$, the two effects described previously coexist when β is increased, as shown by the isocontours of $V_{\rm sat}$ in figure 5. For instance, when $La = 1$, $V_{\rm sat}$ first decreases as β increases, and when the elastic stress is strong enough, the flow is reversed and the discontinuous transition occurs. Note that, in the latter case, inertia is important since La is of order unity, and a small but finite satellite droplet exists in the clean limit, $\beta \to 0$ (see e.g. the second row of figure 4), where $V_{\rm sat} = 0.394$ % (a value significantly larger than in the limit $La \ll 1$, as shown in the isocontours of figure 5). Hence, the main difference with respect to the limit $La \gg 1$ is that in this case, since $V_{\rm sat}(\beta \to 0)$ is small, the increase of β reduces the satellite volume and may even make it negligible. For

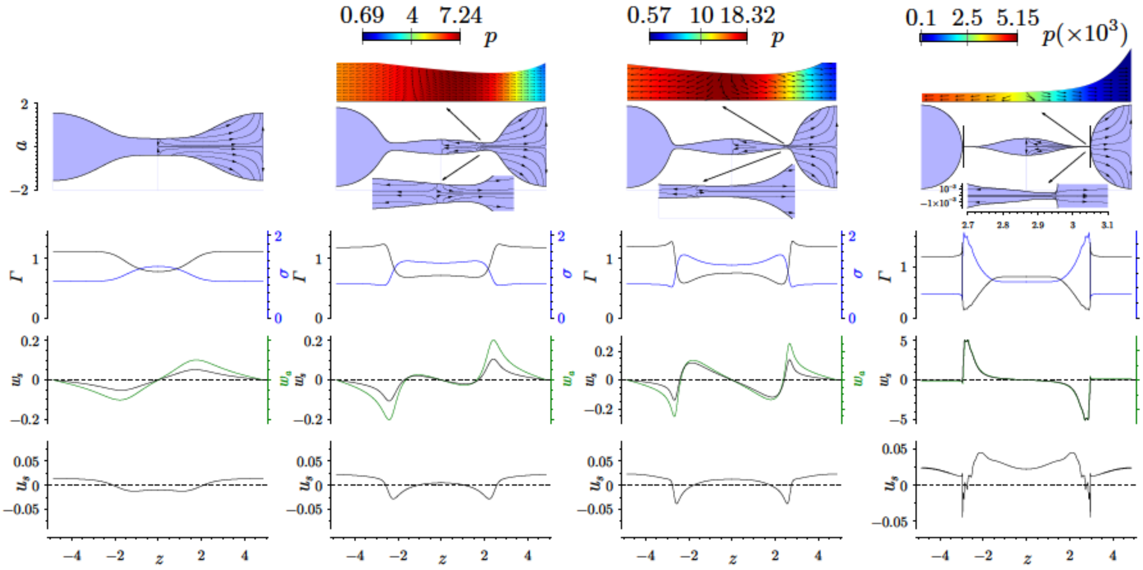

(*a*) $t = 290$ (*b*) $t = 304.5$ (*c*) $t = 307.5$ (*d*) $t = 309.53$

Figure 11: (Colour online) Same as figure 10 but for $\beta = 1$ with $k = k_m = 0.647$. Here $z_{\min} = 2.94$ and $a_{\min} = 5.14 \times 10^{\ 4}$.

$La < 7.5$, Σ_{sat} also decreases monotonically together with V_{sat} when $\beta < \beta_c$, which can be explained by the fact that V_{sat} is already small when $\beta = 0$, so that Σ_{sat} necessarily decreases when β is increased.

Let us recall at this point that the critical elasticity, $\beta_c(La)$, decreases as La increases within the range $0 < La < 7.5$, as shown in figures 3 and 5. The reason for the latter trend is the fact that the advection of surfactant away from the central region is enhanced by the liquid inertia, so that $\boldsymbol{\nabla}_s\sigma$ also increases, and thus the value of β for which the elastic stress reverts the flow is smaller. Furthermore, the value of $V_{\text{sat}}(La, \beta \to 0)$ increases as La becomes larger, and therefore the jumps experienced by V_{sat} and Σ_{sat} at the discontinuous transition, $\beta = \beta_c$, decrease, as deduced from the inset of figure 3. Finally, for $La > 7.5$, the discontinuous transition disappears.

3.3.4. *Scaling laws for V_{sat} and Σ_{sat} as functions of La*

Figure 12 shows V_{sat} and Σ_{sat} as functions of La for different values of β indicated in the legend. The circle with error bars corresponds to the experiment of Rutland & Jameson (1971) of the natural break-up of a liquid jet of clean water, which is in close agreement with our numerical result for $\beta = 0$. The inset displays the most unstable wavenumber, k_m, as a function of La, showing the inviscid plateau $k_m \simeq 0.697$ for $La \gg 1$ (Rayleigh 1878), as well as the power-law dependence for small values of La. The latter power law can be deduced from the long-wave approximation of the dispersion relation (3.2) or, equivalently, from the leading-order one-dimensional model deduced by Eggers & Dupont (1994) and García & Castellanos (1994). In the clean case, $\beta = 0$, the leading-order one-dimensional results are $k_m \sim (2 + 3\sqrt{2}La^{\ 1/2})^{\ 1/2}$ and $\omega_m \sim (2\sqrt{2}+6La^{\ 1/2})^{\ 1}$ (Eggers & Villermaux 2008). The latter long-wave result provides very accurate results in the whole range of La, since $k \in (0, 1)$ accomplishes the slenderness assumption. In the inviscid limit, $La \to \infty$, both ω_m and k_m are slightly overestimated

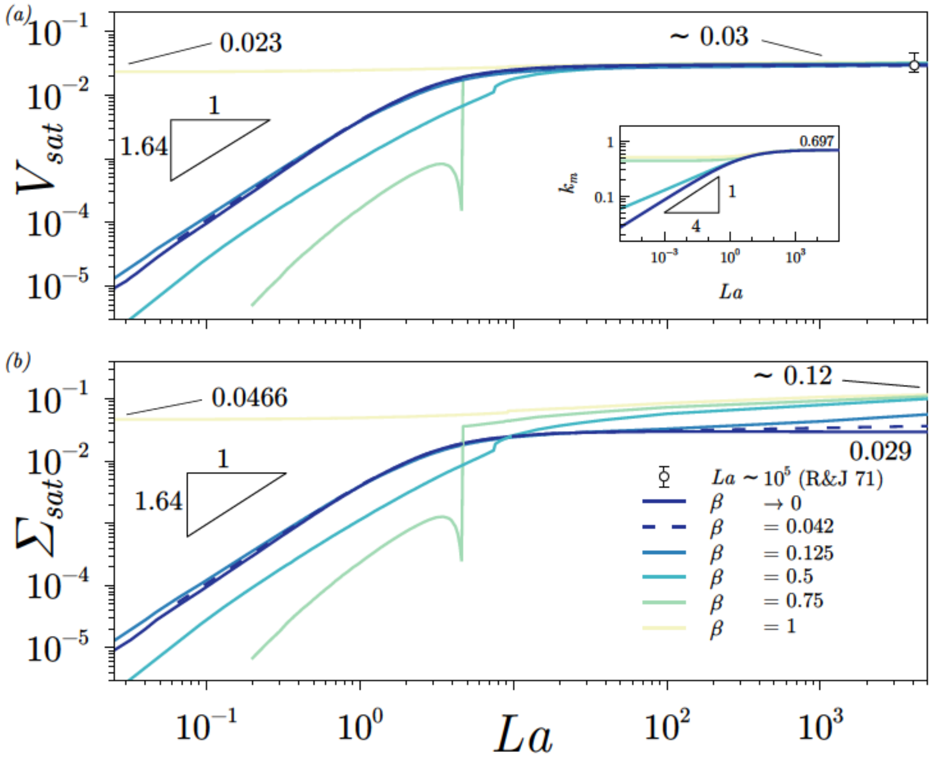

Figure 12: (Colour online) Normalised satellite's volume V_{sat}, and normalised mass of surfactant trapped at its interface $\Sigma_{\rm sat}$, as a function of the Laplace number La in log-log for different values of β indicated in the legend. The inset shows the dependence of the maximum amplification wavenumber k_m with respect to La in log-log. The circle with error bars corresponds to the experiments of the natural break-up of a liquid jet of water performed by Rutland & Jameson (1970).

by the one-dimensional model, namely $\omega_m \to 2^{\ 3/2}$ and $k_m \to 2^{\ 1/2}$. However, in the Stokes limit, $La \ll 1$, the values of $\omega_m \to 1/6$ and $k_m = 3^{\ 1/2}2^{\ 1/4}La^{1/4}$ are in excellent agreement with the exact linear theory. When $\beta > 1/2$, the elastic stress regularises k_m in the limit of $La \to 0$, as analysed in detail by Timmermans & Lister (2002) (see also the isocontours of k_m in figure 2*c*).

In the limit of a clean interface, $\beta = 0$, $V_{\rm sat}$ increases monotonically with La, as previously shown in figures 4 and 5, and explained in figure 6. In particular, our numerical results reveals that the satellite volume scales as $V_{\rm sat} = 0.00421La^{1.64}$ when $La \lesssim 2$, and thus $V_{\rm sat} \to 0$ and $\Sigma_{\rm sat} \to 0$ as $La \to 0$. When La is finite, a satellite drop is always formed, since the liquid thread always experiences a transition to the inertial–viscous regime (Eggers 1993; Castrejón-Pita *et al.* 2015) and thus $z_{\rm min}$ moves from $z = 0$ towards higher values when t is close enough to t_b. The elongated satellite droplet formed when $La \ll 1$ can break up into more droplets after pinch-off as it relaxes, depending on the value of La (Notz & Basaran 2004; Castrejon-Pita *et al.* 2012; Wang *et al.* 2019; Anthony *et al.* 2019), unless $La \to 0$ (Eggers & Fontelos 2005). Alternatively, using the expression for the equivalent radius $R_{\rm sat}$ developed in §3.2, which depends on k_m, and since $k_m = 3^{\ 1/2}2^{\ 1/4}La^{1/4}$ within the range of La for which $V_{\rm sat}$ exhibits power-law scaling, it is deduced that $R_{\rm sat} = 0.34La^{0.463}$.

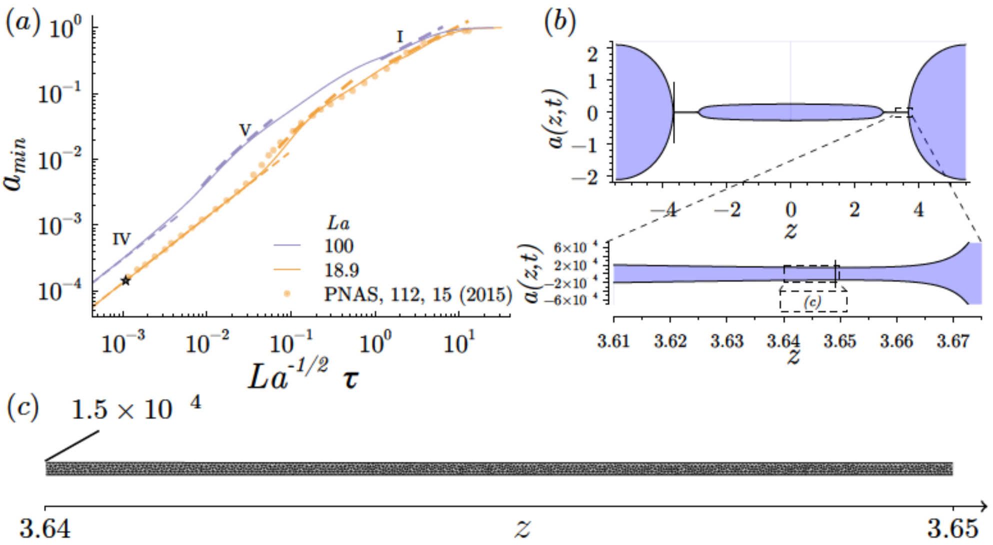

Figure 13: (Colour online) (*a*) Minimum thread radius $a_{\min}$ as a function of the time to break-up τ for two different values of the Laplace number, namely La = 18.9 and 100, and $\beta = 0$. The dashed lines indicate the scaling laws in the different regimes, and the symbols correspond to the results extracted from the numerical simulations of Castrejón-Pita *et al.* (2015). (*b*) Shape of the thread for the case La = 18.9 at t = 138.017, where $a_{\min} = 1.43 \times 10\ ^{4}$ and $z_{\min} = 3.65$, and which corresponds to the star symbol in (*a*) for $\tau = 1.08 \times 10\ ^{3}$. The zoomed region shows the micro-filament formed just prior to pinch-off. (*c*) Local mesh in the micro-filament region.

here for conciseness, we have checked that the unphysical singularity of the equation of state (2.10) as $\Gamma \to 0$ leads to a spurious deviation from the asymptotic IV regime, which precludes its use in correctly predicting the smallest scales prior to pinch-off for $\beta \neq 0$. To that end, a different equation of state that provides the clean-interface constant value of σ as $\Gamma \to 0$ must be used (McGough & Basaran 2006; Kamat *et al.* 2018).

REFERENCES

AMBRAVANESWARAN, B. & BASARAN, O.A. 1999 Effects of insoluble surfactants on the nonlinear deformation and breakup of stretching liquid bridges. *Phys. Fluids* **11** (5), 997–1015.

AMBRAVANESWARAN, B., SUBRAMANI, H.J., PHILLIPS, S.D. & BASARAN, O.A. 2004 Dripping-jetting transitions in a dripping faucet. *Phys. Rev. Lett.* **93**, 034501.

AMBRAVANESWARAN, B., WILKES, E. D. & BASARAN, O. A. 2002 Drop formation from a capillary tube: Comparison of one-dimensional and two-dimensional analyses and occurrence of satellite drops. *Phys. Fluids* **14** (8), 2606–2621.

ANNA, S.L. 2016 Droplets and bubbles in microfluidic devices. *Annu. Rev. Fluid Mech.* **48**, 285–309.

ANTHONY, C. R., KAMAT, P. M., HARRIS, M. T. & BASARAN, O. A. 2019 Dynamics of contracting filaments. *Phys. Rev. Fluids* 4 (9), 093601.

ASHGRIZ, N. & MASHAYEK, F. 1995 Temporal analysis of capillary jet breakup. *J. Fluid Mech.* **291**, 163–190.

BOGY, D.B. 1979 Drop formation in a circular liquid jet. *Annu. Rev. Fluid Mech.* **11**, 207–228.

BOUSSINESQ, J.V. 1913 *J. Ann. Chim. Phys.* **29**, 349.

Campana, D.M. & Saita, F.A. 2006 Numerical analysis of the rayleigh instability in capillary tubes: The influence of surfactant solubility. *Phys. Fluids* **18**, 022104.

Castrejon-Pita, A. A., Castrejon-Pita, J. R. & Hutchings, I. M. 2012 Breakup of liquid filaments. *Phys. Rev. Lett.* **108** (7), 074506.

Castrejón-Pita, J. R., Castrejón-Pita, A. A., Thete, S. S., Sambath, K., Hutchings, I. M., Hinch, J., Lister, J. R. & Basaran, O. A. 2015 Plethora of transitions during breakup of liquid filaments. *Proc. Natl. Acad. Sci. U.S.A.* **112** (15), 4582–4587.

Champougny, L., Scheid, B., Restagno, F., Vermant, J. & Rio, E. 2015 Surfactant-induced rigidity of interfaces: a unified approach to free and dip-coated films. *Soft Matter* **11** (14), 2758–2770.

Chandrasekhar, S. 1961 *Hydrodynamic and Hydromagnetic Stability*. ed and Transl. E MacCurdy (New York: George Brazillier).

Chaudhary, K.C. & Maxworthy, T. 1980 The nonlinear capillary instability of a liquid jet. part 3. experiments on satellite drop formation and control. *J. Fluid. Mech.* **96** (2), 287–297.

Christopher, G.F. & Anna, S.L. 2007 Microfluidic methods for generating continuous droplet streams. *J. Phys. D: Appl. Phys.* **40**, R319–R336.

Craster, R.V., Matar, O.K. & Papageorgiou, D.T. 2002 Pinchoff and satellite formation in surfactant covered viscous threads. *Phys. Fluids* **14** (4), 1364–1376.

Craster, R.V., Matar, O.K. & Papageorgiou, D.T. 2009 Breakup of surfactant-laden jets above the critical micelle concentration. *J. Fluid Mech.* **629**, 195–219.

Day, Richard F, Hinch, E John & Lister, John R 1998 Self-similar capillary pinchoff of an inviscid fluid. *Phys. Rev. Lett.* **80** (4), 704.

Delacotte, J., Montel, L., Restagno, F., Scheid, B., Dollet, B., Stone, H.A., Langevin, D. & Rio, E. 2012 Plate coating: influence of concentrated surfactants on the film thickness. *Langmuir* **28** (8), 3821–3830.

Derby, B. 2010 Inkjet printing of functional and structural materials: Fluid property requirements, feature stability, and resolution. *Annu. Rev. Mater. Res.* **40**, 395–414.

Donnelly, R.J. & Glaberson, W.I. 1966 Experiments on the capillary instability of a liquid jet. *Proc. Roy. Soc.* **A290**, 547–566.

Dravid, V., Songsermpong, S., Xue, Z., Corvalan, C.M. & Sojka, P.E. 2006 Two-dimensional modeling of the effects of insoluble surfactant on the breakup of a liquid filament. *Chem. Eng. Sci.* **61**, 3577–3585.

Eggers, J. 1993 Universal pinching of 3d axisymmetric free-surface flow. *Phys. Rev. Lett.* **71**, 3458.

Eggers, J 1997 Nonlinear dynamics and breakup of free surface flows. *Rev. Mod. Phys.* **69**, 865–929.

Eggers, J. & Dupont, T.F. 1994 Drop formation in a one-dimensional approximation of the Navier-Stokes equation. *J. Fluid Mech.* **262**, 205–222.

Eggers, J. & Fontelos, M. A. 2005 Isolated inertialess drops cannot break up. *J. Fluid Mech.* **530**, 177–180.

Eggers, J. & Fontelos, M. A. 2015 *Singularities: formation, structure, and propagation*, , vol. 53. Cambridge University Press.

Eggers, J. & Villermaux, E. 2008 Physics of liquid jets. *Rep. Prog. Phys.* **71**, 036601.

Fuller, G. G. & Vermant, J. 2012 Complex fluid-fluid interfaces: rheology and structure. *Ann. Rev. Chem. Bio. Eng.* **3**, 519–543.

García, F.J. & Castellanos, A. 1994 One-dimensional models for slender axisymmetric viscous liquid jets. *Phys. Fluids* **6** (8), 2676–2689.

Goedde, E.F. & Yuen, M.C. 1970 Experiments on liquid jet instability. *J. Fluid Mech.* **40** (3), 495–511.

González, H. & García, F.J. 2009 The measurement of growth rates in capillary jets. *J. Fluid Mech.* **619**, 179–212.

Hansen, S., Peters, G.W.M. & Meijer, H.E.H. 1999 The effect of surfactant on the stability of a fluid filament embedded in a viscous fluid. *J. Fluid Mech.* **382**, 331–349.

Kalaaji, A., Lopez, B., Attane, P. & Soucemarianadin, A. 2003 Breakup length of forced liquid jets. *Phys. Fluids* **15**, 2469–2479.

Kamat, P.M., Wagoner, B.W., Thete, S.S. & Basaran, O.A. 2018 Role of marangoni stress during breakup of surfactant-covered liquid threads: Reduced rates of thinning and microthread cascades. *Phys. Rev. Fluids* **3** (4), 043602.

Karapetsas, George & Bontozoglou, Vasilis 2013 The primary instability of falling films in the presence of soluble surfactants. *J. Fluid Mech.* **729**, 123–150.

Keller, J.B., Rubinow, S.I. & Tu, Y.O. 1973 Spatial instability of a jet. *Phys. Fluids* **16**, 2052–2055.

Keller, Joseph B & Miksis, Michael J 1983 Surface tension driven flows. *SIAM J. App. Math.* **43** (2), 268–277.

Kovalchuk, N. M., Jenkinson, H., Miller, R. & Simmons, M. J. H. 2018 Effect of soluble surfactants on pinch-off of moderately viscous drops and satellite size. *J. Colloid Interf. Sci.* **516**, 182–191.

Kowalewski, T. A 1996 On the separation of droplets from a liquid jet. *Fluid Dyn. Res.* **17**, 121–145.

Lafrance, P. 1975 Nonlinear breakup of a laminar liquid jet. *Phys. Fluids* **18** (4), 428–432.

Langevin, D. 2014 Rheology of adsorbed surfactant monolayers at fluid surfaces. *Annu. Rev. Fluid Mech.* **46**, 47–65.

Lee, H.C. 1974 Drop formation in a liquid jet. *IBM Journal of Research and Development* **18** (4), 364–369.

Leib, S.J. & Goldstein, M.E. 1986*a* Convective and absolute instability of a viscous liquid jet. *Phys. Fluids* **29** (4), 952–954.

Leib, S.J. & Goldstein, M.E. 1986*b* The generation of capillary instabilities on a liquid jet. *J. Fluid Mech.* **168**, 479–500.

Liao, Y.C., Franses, E.I. & Basaran, O.A. 2006 Deformation and breakup of a stretching liquid bridge covered with an insoluble surfactant monolayer. *Phys. Fluids* **18** (2), 022101.

Magnus, G. 1859 *Ann. Phys. Chem.* **106**, 1.

Mansour, Nagi N & Lundgren, Thomas S 1990 Satellite formation in capillary jet breakup. *Phys. Fluids A: Fluid Dyn.* **2** (7), 1141–1144.

Martínez-Calvo, A., Rubio-Rubio, M. & Sevilla, A. 2018 The nonlinear states of viscous capillary jets confined in the axial direction. *J. Fluid Mech.* **834**, 335–358.

Martínez-Calvo, A. & Sevilla, A. 2018 Temporal stability of free liquid threads with surface viscoelasticity. *J. Fluid Mech.* **846**, 877–901.

Mashayek, F. & Ashgriz, N. 1995 Nonlinear instability of liquid jets with thermocapillarity. *J. Fluid Mech.* **283**, 97–123.

McGough, P.T. & Basaran, O.A. 2006 Repeated formation of fluid threads in breakup of a surfactant-covered jet. *Phys. Rev. Lett.* **96** (5), 054502.

Notz, P. K. & Basaran, O. A. 2004 Dynamics and breakup of a contracting liquid filament. *J. Fluid Mech.* **512**, 223–256.

Papageorgiou, D.T. 1995 On the breakup of viscous liquid threads. *Phys. Fluids* **7** (7), 1529–1544.

Pereira, A. & Kalliadasis, S. 2008 On the transport equation for an interfacial quantity. *Eur. Phys. J. Appl. Phys.* **44** (2), 211–214.

Plateau, J. 1873 *Statique expérimentale et théorique des liquides*. Gauthier-Villars et C^{ie}, Paris.

Ponce-Torres, A., Montanero, J.M., Herrada, M.A., Vega, E.J. & Vega, J.M. 2017 Influence of the surface viscosity on the breakup of a surfactant-laden drop. *Phys. Rev. Lett.* **118**, 024501.

Rayleigh, W.S. 1878 On the instability of jets. *Proc. R. Soc. Lond.* **10**, 4–13.

Rayleigh, W.S. 1882 Further observations upon liquid jets, in continuation of those recorded in the royal society's 'proceedings' for march and may. *Proc. R. Soc. Lond.* pp. 130–145.

Rayleigh, W.S. 1892 On the instability of a cylinder of viscous liquid under capillary force. *Phil. Mag. and J. Science* .

Rivero-Rodríguez, J. & Scheid, B. 2018*a* Bubble dynamics in microchannels: inertial and capillary migration forces. *J. Fluid Mech.* **842**, 215–247.

Rivero-Rodríguez, J. & Scheid, B. 2018*b* Bubble dynamics in microchannels: inertial and capillary migration forces – CORRIGENDUM. *J. Fluid Mech.* **855**, 1242–1245.

Roché, M., Aytouna, M., Bonn, D. & Kellay, H. 2009 Effect of surface tension variations on the pinch-off behavior of small fluid drops in the presence of surfactants. *Phys. Rev. Lett* **103** (26), 264501.

Rubio-Rubio, M., Sevilla, A. & Gordillo, J.M. 2013 On the thinnest steady threads obtained by gravitational stretching of capillary jets. *J. Fluid Mech.* **729**, 471–483.

Rutland, D.F. & Jameson, G.J. 1970 Theoretical prediction of the sizes of drops formed in the breakup of capillary jets. *Chem. Eng. Sci.* **25** (11), 1689–1698.

Rutland, D.F. & Jameson, G.J. 1971 A non-linear effect in the capillary instability of liquid jets. *J. Fluid Mech.* **46** (2), 267–271.

Savart, F. 1833 Mémoire sur la constitution des veines liquides lancées par des orifices circulaires en mince paroi. *Ann. Chim.* **53**, 337–386.

Scheid, B., Delacotte, J., Dollet, B., Rio, E., Restagno, F., van Nierop, E.A., Cantat, I., Langevin, D. & Stone, H.A. 2010 The role of surface rheology on liquid film formation. *EPL* **90**, 24002.

Scriven, L.E. 1960 Dynamics of a fluid interface. Equation of motion for Newtonian surface fluids. *Chem. Eng. Sci.* **12** (2), 98–108.

Siderius, A., Kehl, S. K. & Leaist, D. G. 2002 Surfactant diffusion near critical micelle concentrations. *J. Solution Chem.* **31** (8), 607–625.

Stone, H.A. 1990 A simple derivation of the time-dependent convective-diffusion equation for surfactant transport along a deforming interface. *Phys. Fluids A* **2** (1), 111–112.

Subramani, H.J., Yeoh, H.K., Suryo, R., Xu, Q., Ambravaneswaran, B. & Basaran, O.A. 2006 Simplicity and complexity in a dripping faucet. *Phys. Fluids* **18** (3), 032106.

Timmermans, M.-L. & Lister, J.R. 2002 The effect of surfactant on the stability of a liquid thread. *J. Fluid Mech.* **459**, 289–306.

Wang, F., Contò, F. P., Naz, N., Castrejón-Pita, J. R., Castrejón-Pita, A. A., Bailey, C. G., Wang, W., Feng, J. J. & Sui, Y. 2019 A fate-alternating transitional regime in contracting liquid filaments. *J. Fluid Mech.* **860**, 640–653.

Whitaker, S. 1976 Studies of the drop-weight method for surfactant solutions III. Drop stability, the effect of surfactants on the stability of a column of liquid. *J. Colloid Interf. Sci.* **54** (2), 231–248.

Wong, H., Rumschitzki, D. & Maldarelli, C. 1996 On the surfactant mass balance at a deforming fluid interface. *Phys. Fluids* **8** (11), 3203–3204.

Xu, Q., Liao, Y.-C. & Basaran, O.A. 2007 Can surfactant be present at pinch-off of a liquid filament? *Phys. Rev. Lett.* **98** (5), 054503.

Yildirim, O. E., Xu, Q. & Basaran, O. A. 2005 Analysis of the drop weight method. *Phys. Fluids* **17**, 062107.

Yuen, M.-C. 1968 Non-linear capillary instability of a liquid jet. *J. Fluid Mech.* **33** (1), 151–163.